Title
Design Principles for High-Capacity Mn-Based Cation-Disordered Rocksalt Cathodes

Journal
Chem, 6(1)

ISSN
2451-9308

Authors
Lun, Z
Ouyang, B
Cai, Z
et al.

Publication Date
2020-01-09

DOI
10.1016/j.chempr.2019.10.001

Peer reviewed

Design principles for high-capacity Mn-based cation-disordered rocksalt cathodes

CHEMJOURNAL-D-19-00749

~~(Revised parts in the manuscript are highlighted in yellow)~~

Zhengyan Lun [†ab], Bin Ouyang [†ab], Zijian Cai [ab], Raphaële J. Clément [a#], Deok-Hwang Kwon [a], Jianping Huang [b], Joseph K. Papp [d], Mahalingam Balasubramanian [c], Yaosen Tian [ab], Bryan D. McCloskey [de], Huiwen Ji [abe], Haegyeom Kim [b], Daniil A. Kitchaev [#], Gerbrand Ceder [ab*@]

[a] Department of Materials Science and Engineering, UC Berkeley, Berkeley, CA 94720, USA

[b] Materials Sciences Division, LBNL, Berkeley, CA 94720, USA

[c] X-ray Science Division, Advanced Photon Source, Argonne National Laboratory, Argonne, IL 60439, USA

[d] Department of Chemical and Biomolecular Engineering, UC Berkeley, Berkeley, CA 94720, USA

[e] Energy Storage and Distributed Resources Division, LBNL, Berkeley, CA 94720, USA

[#] Present address: Materials Department, University of California, Santa Barbara, CA 93106, USA

[†] These authors contributed equally.

[*] Email: gceder@berkeley.edu

[@] Lead contact

Summary

Mn-based Li-excess cation-disordered rocksalt (DRX) oxyfluorides are promising candidates for next-generation rechargeable battery cathodes owing to their large energy densities, earth-abundance of Mn and potential for low cost. In this work, we synthesized and electrochemically tested four representative compositions in the Li–Mn–O–F DRX chemical space with various Li and F conteWhile all compositions tested achieve higher than 200 mAh g^{-1} material with high Li-excess (1.3333 per formula unit, $Li_xMn2\text{-}_xO2\text{-}_yF_y$) and moderate fluorination (0.3333 per formula unit) achieves 349 mAh g^{-1} initial capacity and 1068 Wh Higher fluorination (0.6667 per formula unit) at moderate Li-excess (1.25 per formula unit) can activate Mn^{2+}/Mn^{4+} redox and there by balance capacity with cycle life, Wh/kg) initial capacity (specific energy) with more than 85% retained after 30 cycles. We show that the Li-site distribution (i.e., Li percolation properties) plays a more important role than the metal-redox capacity in determining the initial capacity, whereas the metal-redox capacity is more closely related to the cyclability of the materials. We apply these insights and generate a capacity map of the Li–Mn–O–F chemical space, $Li_xMn2\text{-}_xO2\text{-}_yF_y$ ($1.167 \leq x \leq 1.333$, $0 \leq y \leq 0.667$), which predicts both the accessible Li capacity and Mn-redox capacity. This map allows to design compounds which balance high capacity with good cyclability.

Keywords

Cation-disordered rocksalt cathodes, Li-excess Mn-based oxyfluorides, short-range order, density functional theory, Monte-Carlo simulation, Li percolation, fluorination

1 Introduction

2 The tremendous success and growth of Li-ion based energy storage in a broad range of

3 applications[1,2] is likely to strain our natural resources[3]. Projected growth of Li-ion production

4 towards 1 TWh/year will require more than a million tons of Co/Ni combined, which constitutes

5 a very sizeable fraction of the annual production of these metals [4]. The recent development of Li-

6 excess cation-disordered rocksalt (DRX) cathodes[5,6,7] is providing an avenue for the Li-ion battery

7 field to develop high energy density cathodes with more abundant and less expensive metals. In

8 these DRX compounds Li migrates through a percolating network of so called '0-TM' clusters in

9 which the absence of transition metals at the activated state enables facile migration[5,6]. Lifting the

10 restriction that cathode structures must be layered and remain layered during electrochemical

11 cycling has enabled the exploration of a much wider chemical space beyond the traditional Ni-Co-

12 Mn (NCM) space [5,8-17]. In addition, the ability to substitute some of the oxygen by fluorine in

13 locally Li-rich environments in DRX structures provides an extra handle to optimize performance

14 by introducing additional metal-redox capacity [8,15,18] and improve cyclability [13,18].

15 Mn is a particularly promising redox active element for cathodes because of its low cost and natural

16 abundance. In addition, fully charged Mn-cathodes contain Mn^{4+} which is a stable valence state

17 thereby enhancing the thermal stability of cathode materials. The Mn^{3+}/Mn^{4+} redox

couple is

18 active in LiMn2O4 spinel cathodes but can only be partially utilized because of the collective Jahn-

19 Teller distortion upon full reduction to Mn^{3+} [19]. Recently, the highly F-substituted DRX

20 compounds Li2Mn2/3Nb1/3O2F and Li2Mn1/2Ti1/2O2F were shown to have very high capacity with

21 two electron Mn2+ to Mn4+ oxidation8. Other high capacity Mn-compounds include Li4Mn2O5,

22 which was argued to utilize a combination of Mn^{3+}/Mn^{4+}, O^{2-}/O^{-}, and Mn^{4+}/Mn^{5+} redox, but

23 experiences severe capacity fading upon extended cycling10. In Li1.9Mn0.95O2.05F0.95, partial

fluorine substitution was applied to improve cyclability[15]. In another example, V^{4+} was applied as a charge compensator in $Li_{1.171}Mn_{0.343}V_{0.486}O_{1.8}F_{0.2}$ to obtain additional electron capacity from the V^{4+}/V^{5+} redox in addition to that provided by the Mn^{2+}/Mn^{4+} redox [14].

These initial results demonstrate that the Li–Mn–O–F chemical space may be particularly important for finding high-capacity, low cost cathodes. Optimization of these materials is likely to involve several tradeoffs: The Li-excess required for good transport in disordered rocksalts reduces the transition metal electron capacity, necessitating oxygen redox to achieve high capacity.

Fluorine substitution on anion sites can negate this to some extent by lowering the average valence requirement on the cations. At the same time, F incorporation is expected to change the Li percolation network due to the large bonding preference between Li and F over Mn and F [20]. In this paper we systematically investigate the role of each compositional handle (Li excess, transition metal redox capacity, and F-content) on the initial discharge capacity and cycle life within the compositional space $Li_xMn_{2-x}O_{2-y}F_y$ ($1.167 \leq x \leq 1.333$, $0 \leq y \leq 0.667$). We use ab-initio simulations to study how Li percolation is modified by short-range order (SRO), previously shown to significantly affect the Li environments, their percolation, and ultimately the Li-transport of DRX materials [21-24], and correlate it to measured electrochemical performance and spectroscopic information.

18 We synthesize, characterize, model, and electrochemically test four well-chosen compositions

19 within the Li–Mn–O–F DRX chemical space with different Li content and F content: 20 $Li_{1.3333}Mn(III)_{0.6667}O_{1.3333}F_{0.6667}$, $Li_{1.3333}Mn(III)_{0.5}Mn(IV)_{0.1667}O_{1.5}F_{0.5}$, 21 $Li_{1.3333}Mn(III)_{0.3333}Mn(IV)_{0.3333}O_{1.6667}F_{0.3333}$, and $Li_{1.25}Mn(II)_{0.1667}Mn(III)_{0.5833}O_{1.3333}F_{0.6667}$,

22 hereafter referred to as HLF67, HLF50, HLF33, LLF67, respectively, with ‘HL’ referring to ‘high

23 lithium content’ (1.3333 per f.u.), ‘LL’ referring to ‘low lithium content’ (1.25 per f.u.) and

numbers denoting the F content. For one group of samples, the lithium content is kept the same and the F content is gradually decreased from HLF67, HLF50 and HLF33, so that progressively less TM redox capacity is expected because of the incorporation of more Mn^{4+} ions in the as-synthesized material to maintain charge balance. For the other group, HLF67 and LLF67 are used to contrast Li-capacity versus TM capacity. These samples have the same F content, but Li-excess is lowered in LLF67 in order to create more Mn^{2+} giving more transition metal (TM) redox capacity. The redox behavior of these compounds is investigated combining spectroscopic methods and density functional theory (DFT) calculations, while SRO in the materials is studied using a combined DFT and Monte Carlo method. Our investigations reveal that the nature of the Li network and its percolation properties play a more important role than the metal-redox capacity in determining the initial capacity of the compounds, whereas the metal-redox capacity has a greater effect on the capacity retention. We then apply these insights and expand our computational analysis to a larger compositional space within the Li–Mn–O–F chemistry and construct a capacity map to provide more practical guidance for experimental design.

Results

Structural characterization

The four compounds were synthesized using a mechanochemical ball-milling method (see methodology). The X-ray diffraction (XRD) patterns shown in Figure 1a confirm that all the materials form a DRX structure with no observable impurity peaks. In addition, elemental analysis confirmed that the compositions of the materials are close to the target compositions, as shown in Table S1. The difference in lattice constants of the materials is consistent with the degree of Mn oxidation. The presence of more Mn^{4+} reduces the lattice constant from

to 4.1477±0.0005 Å (HLF50) and 4.1184±0.0005 Å (HLF33), whereas the introduction of large

Mn^{2+} ions increases the lattice constant to 4.2141±0.0009 Å for LLF67,

Li content. The F to O ratio appears less significant in determining the lattice constant, consistent

with their small difference in ionic radius [25]. Detailed refinements of the XRD patterns are

presented in Figure S1. Transmission electron microscopy (TEM) electron diffraction (ED)

patterns of the as-synthesized materials also show phase-pure DRX without observable impurities

(Figure 1b, S4). Nanosized small grains with different orientations pack closely together to form

a polycrystalline primary particle (Figure S4), the size of which is in the range of 100–200 nm for

as-synthesized materials, as observed in the scanning electron microscopy (SEM) images in Figure

S2.

Although no LiF impurity phases were detected using XRD and TEM ED techniques, we called

on ^{19}F solid-state nuclear magnetic resonance spectroscopy (ssNMR) to further confirm that most

of the fluorine is incorporated within the bulk material rather than forming a separate LiF phase.

The ^{19}F NMR spectra collected on HLF67, HLF50 and LLF67 powders, as well as on LiF powder

and an empty rotor for reference, are presented in Figure 1c. While the small shoulder at

approximately −163 ppm originates from the probe background, we find that the ^{19}F NMR spectra

collected on the various cathode materials differ significantly from that of the LiF

reference. The

18 former spectra are composed of a number of broad, overlapping signals shifted away from the

19 resonance frequency of LiF at −204 ppm. As discussed in previous NMR studies on related

20 oxyfluoride materials [8,13,14,18,26], these broad features arise from strong paramagnetic interactions

21 from short-range paramagnetic interactions between unpaired *d* electrons on Mn ions and the F

22 nucleus, which confirms the bulk incorporation of F into the disordered rocksalt phase.[6] When F

23 is directly bonded to Mn ions, paramagnetic interactions are so strong that the resulting signals

are too broad to be detectable and are lost in the background noise. These invisible paramagnetic

F sites prevent us from quantifying the fraction of F in LiF-like domains or particles in the pristine

cathode samples, as evidenced by the sharp signal centered at −204 ppm and present in all spectra.

Nevertheless, the present data indicate that the vast majority of the fluorine of the as-synthesized

materials is incorporated into the particles. ^{7}Li NMR spectra are also presented in Figure S3.

Supplementary Note 1 discusses the problem of attributing the ~0 ppm signal to either impurities

or to the possible formation of diamagnetic Li-rich (Mn-poor) domains within the disordered oxide

matrix. Finally, TEM energy dispersive spectroscopy (EDS) mapping images are shown in Figure

1d and S4 and indicate a homogeneous distribution of F throughout the particles, which further

confirms the bulk substitution of F.

Electrochemical performance

The electrochemical performance of the Li–Mn–O–F compounds was tested in galvanostatic mode

at 20 mA g^{-1} and room temperature within different voltage windows (1.5 – 4.6/4.8/5.0 V). Figure

2a summarizes the first cycle discharge capacities, average voltage, and specific energies for all of

the compounds. Figure 2b presents the voltage profiles of HLF67, HLF50, HLF33, and LLF67 for

the first cycle between 1.5 – 4.8V; the compounds exhibit discharge capacities (specific energies)

of 259 mAh g^{-1} (844 Wh kg^{-1}), 284 mAh g^{-1} (909 Wh kg^{-1}), 336 mAh g^{-1} (1059 Wh kg^{-1}), and 242 mAh g^{-1} (771 Wh kg^{-1}), respectively. When cycling between 1.5 – 5.0V, their initial discharge capacities (specific energies) increase to 290 mAh g^{-1} (950 Wh kg^{-1}), 319 mAh g^{-1} (1016 Wh kg^{-1}), 349 mAh g^{-1} (1068 Wh kg^{-1}), and 256 mAh g^{-1} (822 Wh kg^{-1}), respectively, as shown in Figure 2c.

Figure 2d–f present the representative voltage profiles for HLF67, HLF33 and capacity retention, when cycling between 1.5 and 5.0 V. The red dashed lines theoretical Mn-redox capacities in each compound. HLF67 exhibits an initial energy) of 290 mAh g^{-1} (950 Wh kg^{-1}) and good capacity retention (Figure larger initial capacity (specific energy) of 349 mAh g^{-1} (1068 Wh kg^{-1}) but capacity retention compared to that of HLF67 (Figure 2e). LLF67 shows a (specific energy) of 256 mAh g^{-1} (822 Wh kg^{-1}) compared to HLF67 but with less than 15% capacity fading over the first 30 cycles (Figure 2f). More cycling results are presented in Figure S5.

In order to understand the relation between composition and redox mechanism and local SRO in these compounds are carefully studied in sections.

Redox mechanism

The redox mechanisms of the Li–Mn–O–F compounds were investigated using *ex-situ* hard X-ray absorption spectroscopy (XAS) and *ab-initio* calculations. The top panel of Figure 3a shows the Mn K-edge X-ray near-edge structure (XANES) of all four pristine compounds. The Mn K-edge energy increases in the order of LLF67 < HLF67 < HLF50 < HLF33. At the top of charge, the Mn^{3+} / Mn^{4+} redox process is almost complete in HLF50 and HLF33, while Mn ions in HLF67 and LLF67 are oxidized to a lesser extent, as shown in the lower panel of Figure 3a. This finding is consistent with the observation by Lee *et al.* that a large lattice constant and the presence of more

22 Mn-F bonds create more overlap between Mn and O redox and can prevent Mn from being fully

oxidized to Mn^{4+}. [8] These interpretations are further supported by the Mn pre-edge derivative analysis, as presented in Figure S6 and Supplementary Note 2.

To compare the oxidation behavior of Mn in HLF67 and LLF67, we select five points at different states of charge in the first charge: the pristine state, and charged to 3.5 V, 4.2 V, 4.6V, and 5.0 V, respectively, as shown in Figure 3b. In general, similar redox behavior is observed for the two compounds: Mn oxidation dominates at low voltage, but at high voltage, the Mn K-edge barely shifts, indicating limited Mn redox. However, a small shift of the edge position to a lower energy at high voltage is observed in HLF67 but not in LLF67; this shift has been ascribed to the partial reduction of the TM (Mn in this case) due to oxygen oxidation [27]. Partial reduction of Mn at high voltage is also observed in HLF50 and HLF33, as shown in Figure S7a and S7b, which suggests that the participation of oxygen redox processes in the overall charge compensation mechanism is more significant in HLF67, HLF50 and HLF33 than in LLF67.

To obtain further insight into the oxidation mechanisms in these cathode materials, we used density functional theory (DFT) to calculate the voltage curves and the evolution of Mn and O oxidation states upon delithiation. Figure 3c and 3d show the calculated redox mechanism for HLF67and LLF67. It is clear that oxygen redox happens earlier in HLF67 than in LLF67 and contributes more to the overall capacity, consistent with the presence of more Li-excess in HLF67 to facilitate

oxygen oxidation [28]. As a result, Mn partial reduction is observed in HLF67 at the top of charge but not in LLF67. At the top of charge, Mn is less oxidized in LLF67 than in HLF67, which is consistent with the XAS observations.

Combining the electrochemical performance and the redox center data establishes a clear correlation between the charge compensation process and the capacity retention of the compounds: with an increasing contribution of oxygen redox from LLF67 to HLF67, HLF50 and HLF33, the

capacity retention of the materials gradually decreases. Oxygen redox is lead to less stable cycling compared to metal redox since it triggers leaving behind a metal densified surface layer, which hinders Li transport. effective way to lower the average cation oxidation states, enabling the metal redox to improve the capacity retention. Consistently, the amount of is reduced in the order of HLF33 > HLF50 > LLF67, as can be observed electrochemical mass spectroscopy (DEMS) results (shown in Figure S8).

Short-range order (SRO) analysis

The SRO in the Li–Mn–O–F compounds was investigated using a cluster expansion Hamiltonian parameterized by DFT total energy calculations. As the Li network significantly affects the electrochemical performance of DRX compounds [23], we first evaluate the frequency of tetrahedra that are only occupied by Li ions (the 0-TM Li4 tetrahedra) in the four compounds as this is the environment through which Li migrates. Figure 4a shows the fraction of tetrahedra that are 0-TM in the simulated Li–Mn–O–F compounds at 2573K as well as in the random limit (infinite temperature). As calibrated in previous work [20] the temperature of 2573K was chosen as a proxy for the high energy conditions with which disorder is generated with ball milling in the Li–Mn–O–F chemical space but should not be taken as a particularly significant value. The 'Random limit' cation configuration in the structure is one where the cations are distributed over the cation lattice, only satisfying the concentration requirement. Such a

SRO and can be used as a reference. Comparing the 0-TM occurrence in HLF67, HLF50, and HLF33, it is clear that fluorination generally leads to a higher number of tetrahedra being occupied with Li4. This is consistent with the previously established idea that a F- anion in DRX materials

wants to maximize the Li content around it [20,21]. The Li-rich octahedra around F^- predispose the tetrahedra with which they share three cations to be Li4. The ability of F- to create more Li4 tetrahedra is clear when comparing LLF67 which has a larger fraction of them than HLF33, despite containing less Li. However, good Li transport requires connectivity of these Li4 tetrahedra and this is where F seems to have the largest perturbing effect. Figure 4b presents the amount of Li connected to the percolating network. Lowering the F content from HLF67 to HLF50, and HLF33, increases the amount of percolating Li despite the fact that the fraction of Li4 tetrahedra decreases.

These trends with F-content indicate that F modifies the connectivity of the Li4 tetrahedra in a very significant way. Li diffusion throughout the bulk materials only benefits from Li4 tetrahedra that create an efficient percolating network through the material. Highly localized Li clusters, for example where one Li is shared by five 0-TM tetrahedrons or more (as illustrated in Figure 4c), will trap a lot of Li within small domains and prevent the formation of an extended network of 0-TM tetrahedra, thus reduce the ‘efficiency’ of 0-TM connectivity. Figure 4d shows the fraction of Li in Li4 tetrahedra in all compounds, where the different Li environments are classified according to the number of 0-TM units around a central Li. Both “isolated” or highly shared Li ions are detrimental for transport as they have limited contributions to the overall percolation. We can see

17 that in HLF67 and LLF67, a larger fraction of 0-TM Li is shared by more than five 0-TM units,

18 whereas for HLF50 and HLF33, a larger fraction of the 0-TM Li is shared by two to four 0-TM

19 units, which is a more ‘efficient’ way to connect all the 0-TM tetrahedrons. The influence of

20 different Mn valence states on the distribution of F is also investigated, but proven to be less

21 important than the competition between Li-F and Mn-F, as discussed in Figure S9 and

22 Supplementary Note 3. The correlation between discharge capacity changes and the 0-TM

percolating Li fraction in Fig 4b shows that this percolation behavior, rather than just simply the amount of Li4 tetrahedra, is the relevant factor that controls initial capacity.

Equipped with an enhanced understanding of the charge compensation process and Li-transport property in these Li–Mn–O–F compounds, we discuss in the next section the trade-offs between initial capacity and capacity retention, and rationalize some general design principles in a practical compositional space $Li_xMn2\text{-}_xO2\text{-}_yF_y$ ($1.167 \leq x \leq 1.333$, $0 \leq y \leq 0.667$).

Discussion

Transition metal redox capacity and Li-site distribution

Figure 5a summarizes the theoretical Li/Mn capacities, accessible 0-TM capacities predicted by MC simulations, and experimental capacities obtained from the first charge/discharge at 20 mA g^{-1} within the voltage window of 1.5–4.8 V for the Li–Mn–O–F compounds. Although both the TM capacity and Li-site distribution can significantly affect the cycling performance of Li–Mn–O–F compounds, their effects appear in different manner. Comparing HLF67, HLF50, and HLF33, we observe that by increasing the amount of 0-TM percolating Li, the initial charge/discharge capacity of the compounds increases, even though the Mn-redox capacity decreases. This trend is further confirmed by the LLF67 compound which has the lowest theoretical Li capacity and highest Mn-redox capacity but delivers the lowest initial charge/discharge capacity. These results

indicate that the initial capacity does not depend on the Mn-redox capacity but is more related to the Li percolation properties. However, the Mn capacity does strongly influence the capacity decay of the materials upon extended charge-discharge cycling. As observed in Figure 2 and Figure S5, the capacity retention improves in the order HLF33 < HLF50 < HLF67 < LLF67, consistent with the increase of Mn redox capacity. To strengthen our hypothesis, we selected two additional compositions: DRX-Li2MnO3, which has more than 95% of its Li ions in the percolating network,

based on our calculation, and Li1.1667Mn(II)0.3333Mn(III)0.5O1.3333F0.6667 (denoted as L167F67), with a high theoretical Mn-redox capacity which matches its theoretical Li capacity. Both materials were synthesized using a similar mechanochemical ball-milling method described for the other samples. The voltage profiles (first cycle) and cyclability of both compounds together with those of the four previously studied compounds are presented in Figure 5b and 5c, respectively. We can see that DRX-Li2MnO3 exhibits the highest initial charge capacity but worst capacity retention, whereas L167F67F displays the opposite behavior, consistent with our analysis that Li percolation controls initial capacities while Mn redox content controls capacity retention.

Based on these insights, we generate in Figure 5d a capacity map for Li–Mn–O–F compounds as function of the Li excess content (x-axis) and fluorine content (y-axis). The color scale gives the calculated total amount of percolating Li per formula unit (f.u.) at each composition and the solid lines indicate the theoretical Mn-redox capacity. Ideally, a material would have high amount of percolating Li as well as high Mn-redox capacity, but the Fig.5d shows that there is clearly a trade-off between these two. Along the *x*-axis Li excess is increased at the cost of Mn-redox capacity leading to a higher fraction of percolating Li. This is expected to increase the initial discharge capacity but with rapid capacity fade. The percolation properties as a function of F content with fixed Li-excess behave in a more complicated manner. In general, upon increasing F

content at

fixed Li-excess, the fraction of percolating Li decreases initially but then increases. This trend

intuitively makes sense: when the fluorination level is low, the presence of F ions attracts Li around

them forming Li-rich clusters which do not percolate because their concentration - determined by

the F content- is not high enough for those Li-rich clusters to connect and percolate through the

sample. When the F content further increases, the Li-rich clusters around F connect together and

the overall percolation improves. The Li-percolation properties as a function of F content are

presented at five different Li-excess levels calculated from Monte Carlo

1.208, 1.25, 1.292, and 1.333 in $Li_xMn2\text{-}_xO2\text{-}_yF_y$, as shown in Figure 5e. The

(marked in red) at which percolation starts to improve with F content

and for x = 1.33 the fraction of percolating Li actually decreases with F

range shown on the map. It is possible that a critical F content can be found

do not consider that range here due to the difficulty in synthesizing the very

materials. This map will be useful in guiding experimental design within the Li–Mn–O–F space to

identify good candidates with both large 0-TM Li capacity and adequate Mn-redox capacity, e.g.

those with metal redox capacity larger than 0.6 e^- per f.u. and percolating Li

0.7 per f.uConsidering the general presence of SRO^{23} and facile oxygen

materials, our general findings within the Li-Mn-O-F DRX chemical space are

valid in other DRX chemical spaces.

Conclusion

In this work, we investigated Li–Mn–O–F DRX oxyfluorides which form a very promising

chemical space to create high energy, resource-light cathodes. We systematically studied four

representative compounds combining electrochemical tests, spectroscopy, and modeling, and

demonstrated reversible capacities between 200 and 350 mAh g^{-1}. We found that the Li-site

distribution plays a more important role in determining the initial capacity, whereas the metal

redox capacity is more important for determining the cyclability of the material. This intrinsic

tradeoff in DRX materials is related to the role of oxygen redox: increasing Li-excess leads to

better Li transport in DRXs, but results in a larger reliance on oxygen redox to achieve high

capacity, thus worse cyclability. Fluorination can compensate for this to some extent by enabling

more metal redox capacity, but its presence modifies the Li network in a significant way. A capacity map, which includes both the Li percolation properties and Mn redox capacities, is presented to provide further guidance for experimental design in this Li–Mn–O–F chemical space.

Experimental procedures

Synthesis

All Li-Mn-O-F compounds were synthesized by mechanochemical ball-milling. Li_2O (Alfa Aesar, ACS, 99% min), MnO (Sigma-Aldrich, 99.99%), Mn_2O_3 (Alfa Aesar, 99%), MnO_2 (Alfa Aesar, 99.9%), and LiF (Alfa Aesar, 99.99%) were used as precursors. Precursors were stoichiometrically mixed according to charge-balance with a Retsch PM 200 Planetary Ball Mill at a rate of 300 rpm for 2 hours. The mixed precursors were then ball-milled at 500 rpm in Argon-filled stainless-steel ball-mill jars, using a Retsch PM 200 Planetary Ball Mill. The duration of ball-mill synthesis for HLF67, HLF50, HLF33, and LLF67 is 40 hours, and for L167F167 and Li_2MnO_3 is 55 hours. The total amount of precursors was 1g. The grinding media were five 10mm (diameter) stainless balls and ten 5mm (diameter) balls.

Electrochemistry

All cathode films were composed of active materials, SUPER C65 (Timcal), and

polytetrafluoroethylene (PTFE, DuPont, Teflon 8A) at a weight ratio of 70:20:10. To make the cathode films, 280 mg active materials and 80 mg SUPER C65 were mixed and shaker-milled for 1 hour in argon atmosphere with SPEX 800M Mixer/Mill, and PTFE was later added and manually mixed with the shaker-milled mixture for 40 minutes. The components were then rolled into thin films inside the glovebox. Commercialized 1M $LiPF_6$ in ethylene carbonate (EC) and dimethyl carbonate (DMC) solution (volume ratio 1:1) was used as electrolyte. Glass microfibers (Whatman)

were used as separator. FMC Li metal foil was used as anode. Coin cells were assembled inside the glovebox and tested on Arbin battery test instrument at room temperature. The loading density of the films was around 3 mg cm^{-2} based on active materials. The specific capacities were then calculated based on the weight of active materials (70%) in the cathode films. Potentiostatic intermittent titration technique (PITT) measurements were conducted on the same electrode for HLF67, HLF50, HLF33, and LLF67 to obtain quasi-equilibrium voltage profiles. All materials were charged from the open-circuit voltages to 4.8 V with a 0.01V step interval, and the voltage was held constant for 1 hour at each step.

Characterization

X-ray diffraction (XRD) patterns for the as-synthesized compounds were collected using a Rigaku MiniFlex diffractometer (Cu source) in a 2θ range of 5°-85°. Rietveld refinement was done with PANalytical X'pert HighScore Plus software. Elemental analysis was performed by Luvak Inc. with direct current plasma emission spectroscopy (ASTM E 1079-12) for lithium, manganese and with an ion-selective electrode (ASTM D 1179-10) for fluorine. Scanning electron microscopy (SEM) images were collected using a Zeiss Gemini Ultra-55 Analytical Field Emission SEM in the Molecular Foundry at Lawrence Berkeley National Lab (LBNL). Scanning transmission electron microscopy (STEM) / energy dispersive spectroscopy (EDS) measurements were

performed on a JEM-2010F microscope in the Molecular Foundry at LBNL. Neutron power diffraction was measured at Nanoscale Ordered Materials Diffractometer (NOMAD) at the Spallation Neutron Source at Oak Ridge National Laboratory. The neutron pair-distribution function (NPDF) refinement was performed using

Solid-state nuclear magnetic resonance (NMR) spectroscopy

^{19}F and ^{7}Li NMR data on the as-synthesized HLF67, HLF50, and LLF67 powder samples were obtained at room temperature using a Bruker Avance 500 MHz (11.7 T) wide-bore NMR spectrometer, at Larmor frequencies of -470.7 MHz and -194.4 MHz, respectively. The spectra were acquired under 50 kHz magic angle spinning (MAS), using a 1.3 mm double-resonance probe, and chemical shifts were referenced against lithium fluoride powder (LiF, $\delta(^{19}F)$ = -204 ppm and $\delta(^{7}Li)$= -1 ppm). Because the resonant frequency range of the ^{19}F nuclei in the as-synthesized HLF67, HLF50, and LLF67 cathodes is larger than the excitation bandwidth of the radio frequency (RF) pulse used in the NMR experiment, nine spin echo spectra were collected for each sample, with the irradiation frequency varied in steps of 250 ppm or 118 kHz from -1200 ppm to 800 ppm. The individual sub-spectra were processed using a zero-order phase correction so that the on-resonance signal was in the absorption mode. The four sub-spectra were then added to give an overall sum spectrum with no further phase correction required. This 'frequency stepping' [31,32], 'spin echo mapping' [33], or 'VOCS' [34] (variable offset cumulative spectrum) methodology provides a large excitation bandwidth with uniform excitation of the broad ^{19}F signals. Individual ^{19}F spin echo spectra were collected using a 90° RF excitation pulse of 1.6 μs and a 180° RF pulse of 3.2 μs at 76.3 W (or 156 kHz), with a recycle delay of 50 ms. For comparison, a spin echo spectrum was collected

on LiF

using similar RF pulses but a longer recycle delay of 14 s. A ^{19}F probe background spin echo

spectrum, acquired under the same conditions as the individual LMVF20 spin echo spectra but on

an empty rotor, revealed the presence of a low intensity background signal.

^{7}Li spin echo spectra were collected on the HLF67, HLF50, and LLF67 cathode powders using a

90° RF pulse of 0.9 µs and a 180° RF pulse of 1.8 µs at 110 W and a recycle delay of 30 ms.

Ex-situ **hard X-ray absorption spectroscopy (XAS)**

The X-ray absorption near edge spectroscopy (XANES) of Mn K-edge was acquired in transmission mode at beamline 20-BM-B in Advanced Photon Source. The incident beam energy was selected using a Si (111) monochromator. The energy calibration was performed by simultaneously measuring the spectra of appropriate metal foil. Harmonic rejection was accomplished using a Rh-coated mirror. All the *ex-situ* samples are electrodes films, composed of active materials, SUPER C65 and PTFE with weight ratio of 70:20:10, and loading density of 5 mg cm^{-2} (based on active materials). They were assembled as coin cells, charged to designated capacities, then disassembled and washed with DMC in glovebox (except for pristine materials). Additional spectra of reference standards were also measured to facilitate the interpretation. The raw data was normalized and calibrated using Athena software[35].

Differential electrochemical mass spectrometer (DEMS) measurement

The custom-built DEMS, cell geometry, and instrument operation is described in previous publications [36-38]. The electrochemical cells used with the DEMS device were prepared in glove box using modified Swagelok design and the cathode film is composed of active materials, carbon black and PTFE with weight ratio of 70:20:10, and loading density of ~10 mg cm^{-2} (based on active materials). The electrolyte, separators, and anodes used were identical to those used for the coin cell tests in this study. The assembled cells were charged at 20 mA g^{-1} under a

static head of

positive argon pressure (around 1.2 bar) at room temperature after being appropriately attached to

the DEMS.

Computational methods

A combination of density functional theory (DFT) calculations together with cluster expansion

Monte Carlo simulations as described in previous reports[14,39] has been applied to understand the

energetics, short range order and Li percolation in LiF-MnO-LiMnO2-Li2MnO3 compositional

space. Using the DFT energy of 1019 structures, a cluster expansion for cation occupancy in the rocksalt structure consisting of pair interactions up to 7.1 Å, triplet interactions up to 4.0 Å, and quadruplet interactions up to 4.0 Å was fitted. The effective cluster interactions and dielectric constant were obtained from a L1-regularized least squares regression[40], with the regularization parameters chosen to minimize cross-validation error[40]. By this procedure, an root-mean-squared error below 7 meV/atom has been obtained.

The DFT calculations have been performed with the Vienna ab-initio simulation package (VASP)[41] and the projector-augmented wave (PAW) method[42]. For each of the structural optimization calculation, a reciprocal space discretization of 25 Å is applied, and the convergence criteria are set as 10^{-6} eV for electronic loops and 0.02 eV/Å for ionic loops. The PBE exchange–correlation functional with the rotationally-averaged Hubbard U correction[43] has been applied for obtaining more accurate DFT energetics, the U parameters are chosen from a previously reported calibration to oxide formation energies[44] (3.9 eV for Mn).

Short range order and percolation information was obtained from canonical Monte Carlo sampling of fully lithiated structure using the Metropolis–Hastings algorithim[45,46]. To guarantee good statistics percolation analysis and short-range order for each composition and temperature are averaged over 500 structures with each consist of 6×6×8 supercells with 576 atoms.

18 To evaluate the voltage curve and redox mechanism, all possible Li-Vacancy ordering in small

19 supercells are enumerated with energies calculated by the SCAN meta-GGA exchange correlation

20 functional[47] which provides a more accurate ranking of structural energetics[48,49]. With energetics

21 evaluated by SCAN, the delithated cluster expansion is then fitted as an offset from a baseline of

22 formal charge electrostatics. The various oxidation states of Mn and O were treated as different

23 species and were identified according from the magnetic moment on these species in the SCAN

calculations. The final root-mean-square error of this cluster expansion is less than 5 meV/atom.

With this cluster expansion, the most stable Li-Vacancy ordering at each delithiation stage has been fully optimized using DFT for constructing the voltage curve. The pymatgen code [50] has been utilized for all the structure analysis and post-processing.

Supplementary information

Supplemental information can be found with the article online at XXXX.

Acknowledgements

This work was supported by the Umicore Specialty Oxides and Chemicals the Assistant Secretary for Energy Efficiency and Renewable Energy, Vehicle Technologies Office, of the U.S. Department of Energy under Contract No. DEAC02-05CH11231, under the Advanced Battery Materials Research (BMR) Program. Work at the Molecular Foundry was supported by the Office of Science, Office of Basic Energy Sciences, of the U.S. Department of Energy under contract No. DE-AC02-05CH11231. The NMR experimental work reported here made use of the shared facilities of the UCSB MRSEC (NSF DMR 1720256), a member of the Material Research Facilities Network. This research used resources of the Advanced Photon Source, an Office of Science User Facility operated for the U.S. Department of Energy (DOE) Office of Science by Argonne National Laboratory, and was supported by the U.S. DOE under Contract No. DE-AC02-

20 06CH11357. This research used resources at the Spallation Neutron Source, a DOE Office of

21 Science User Facility operated by the Oak Ridge National Laboratory. The computational analysis

22 was performed using computational resources sponsored by the Department of Energy's Office of

23 Energy Efficiency and Renewable Energy and located at the National Renewable Energy

Laboratory, computational resources provided by Extreme Science and Engineering Discovery Environment (XSEDE), which was supported by National Science Foundation grant number ACI1053575, as well as the National Energy Research Scientific Computing Center (NERSC), a DOE Office of Science User Facility supported by the Office of Science and the U.S. Department of Energy under Contract No. DE-AC02-05CH11231.The authors thank Dr. Hyunchul Kim and Dr. Nongnuch Artrith for helpful discussion. The authors thank Mr. Jingyang Wang for the help of XAS measurement. The authors thank Dr. Jue Liu for the help of neutron diffraction measurement.

Author contributions

Z.L. planned the project with G.C.; Z.L. designed, synthesized, characterized (XRD) and electrochemically tested the proposed compounds with the help from Z.C., H.J. and H.K.; B.O. performed Monte Carlo and DFT calculations and analyzed the data with the help from D.A.K.; R.J.C. acquired and analyzed the NMR data; Z.L. acquired and analyzed the XAS data with the help from M.B. and J. H.; D.K. acquired and analyzed TEM data; J.K.P. acquired and analyzed DEMS data with input from B.D.M.; Y.T. performed SEM. The manuscript was written by Z.L. and was revised by R.J.C., D.A.K., H.J. and G.C. with the help of the other authors. All authors contributed to discussions.

Declaration of interests

The authors declare no competing interests.

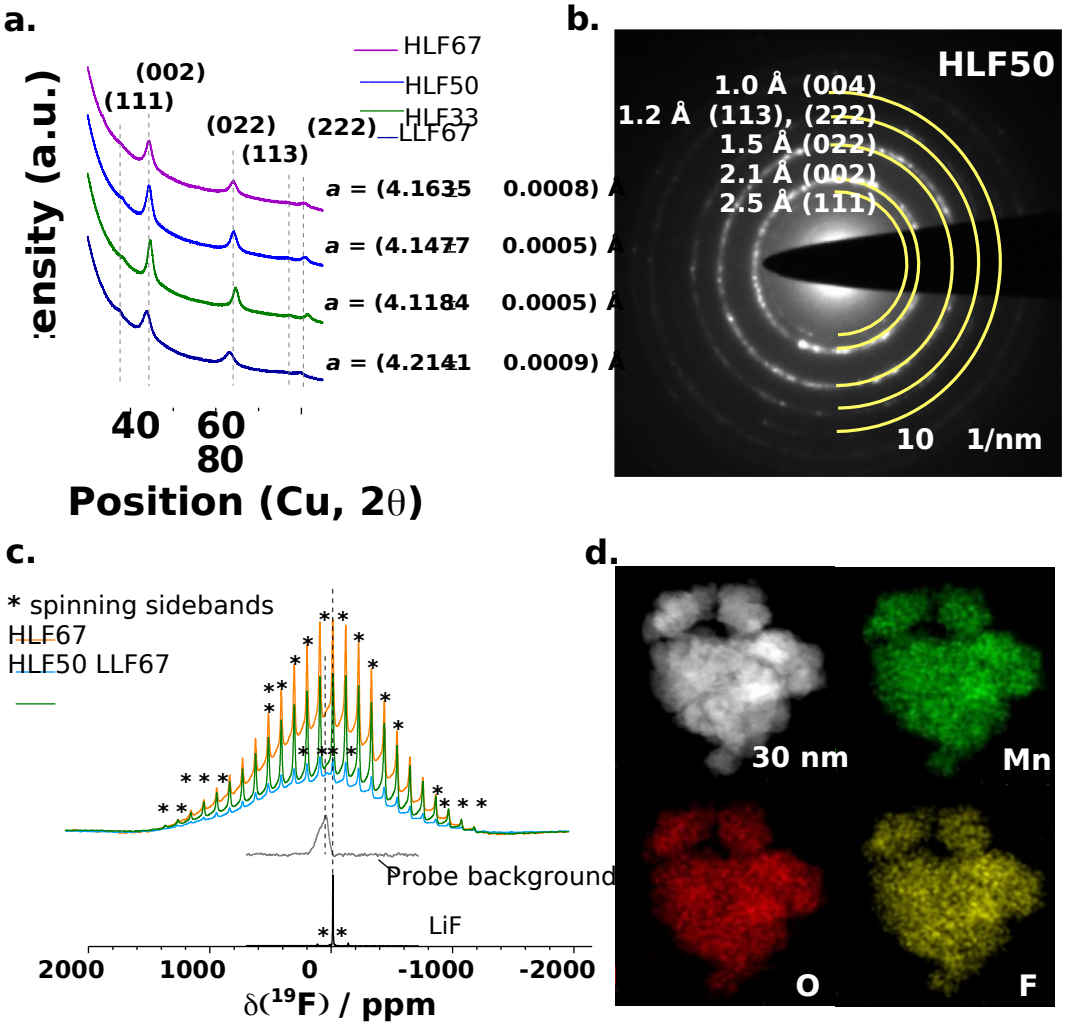

Figure 1 | Structural characterization of the as-synthesized Li-Mn-O-F compounds. a. XRD patterns and refined lattice constants of the as-synthesized materials. **b.** Electron diffraction pattern of as-synthesized HLF50. **c.** ^{19}F frequency-stepping spectra obtained for the as-synthesized HLF67, HLF50, LLF67 powders by summing over nine spin echo sub-spectra acquired at different excitation frequencies. The spectra are scaled according to the amount of sample in the rotor. For comparison, ^{19}F spin echo spectra collected on LiF powder and on an empty rotor (to measure the probe background signal) are overlaid. The shoulder observed to the left of the most intense peak in the spectra, at ca. -163 ppm, is ascribed to the probe background signal. Spinning

sidebands of

the sharp, diamagnetic signals are indicated with asterisks. **d.** TEM/EDS mapping of the elemental

distribution in a particle cluster of as-synthesized HLF50.

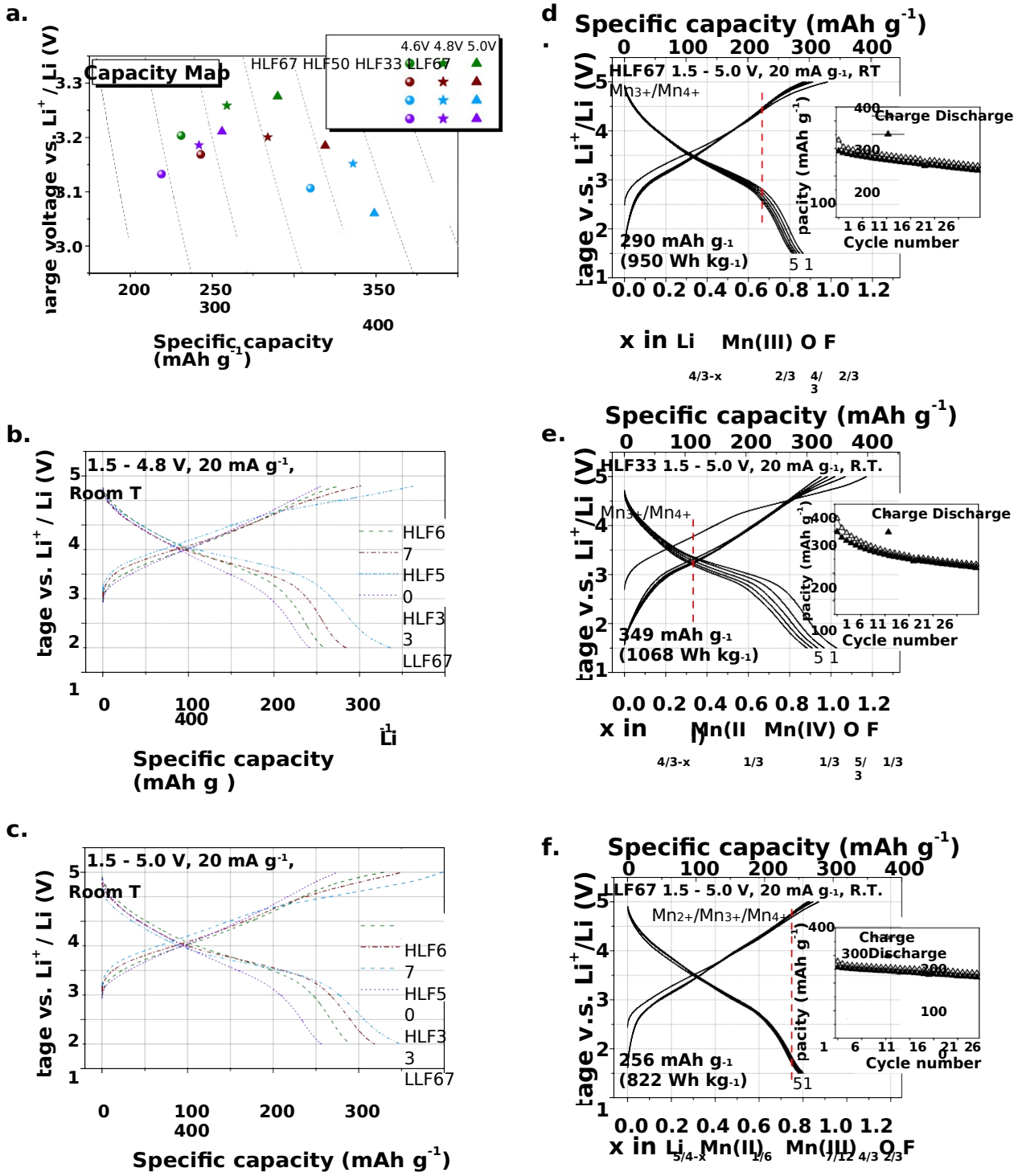

Figure 2 | **Electrochemical performance of Li-Mn-O-F compounds. a.** Capacity map showing

initial discharge capacities and energy densities of Li-Mn-O-F compounds at different voltage windows. First cycle voltage profiles of Li-Mn-O-F compounds within the voltage windows of **b.** 1.5 - 4.8V and **c.** 1.5 – 5.0V at a rate of 20 mA g^{-1} and room temperature. Representative voltage profiles and capacity retention of **d.** HLF67; **e.** HLF33; **f.** LLF67 within the voltage window of 1.5 – 5.0V at 20 mA g^{-1} and room temperature. The red dashed lines indicate the theoretical Mn-redox capacities. The initial oxidation states of Mn in the as-synthesized materials can be found from the bottom x-axis.

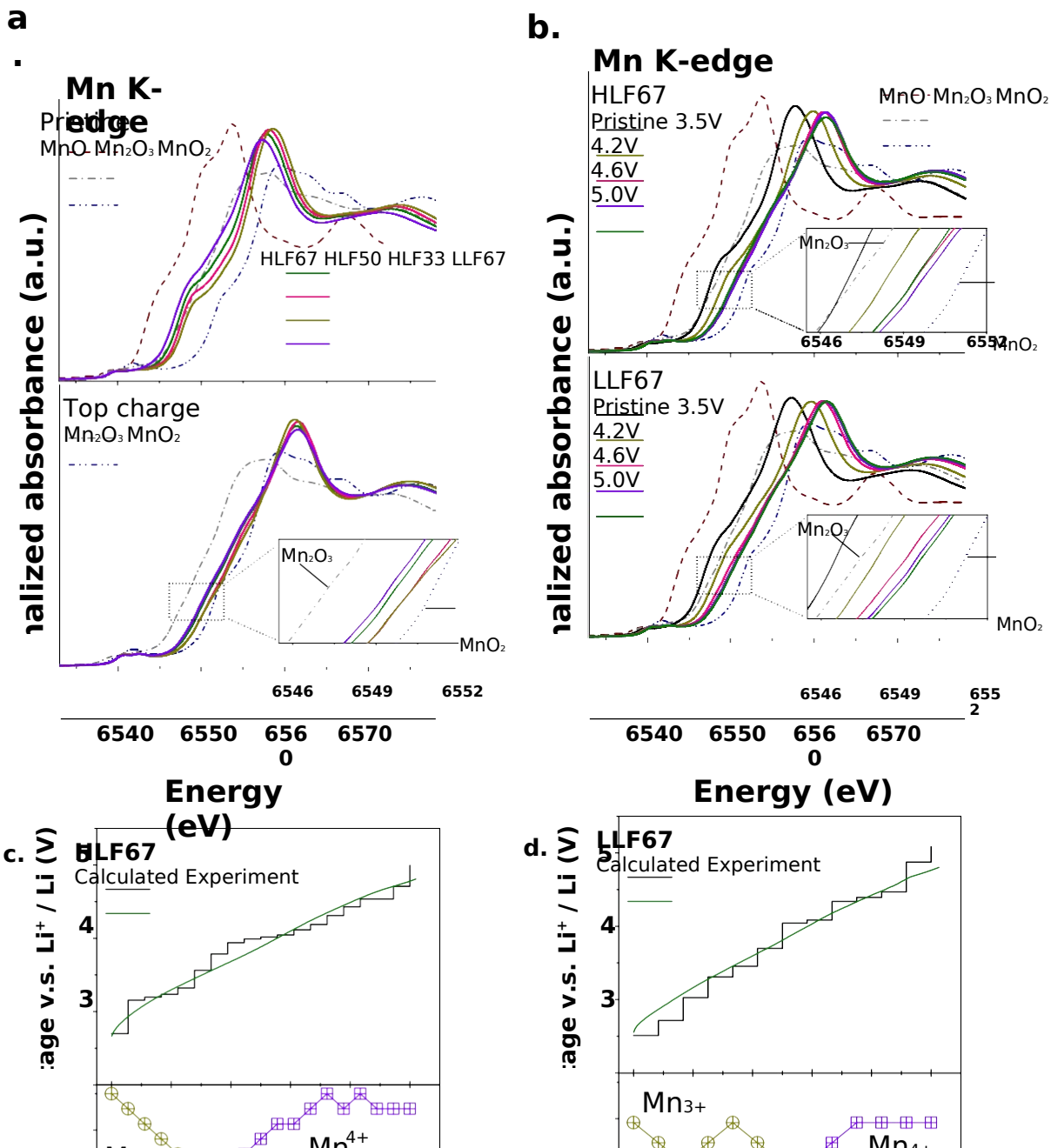

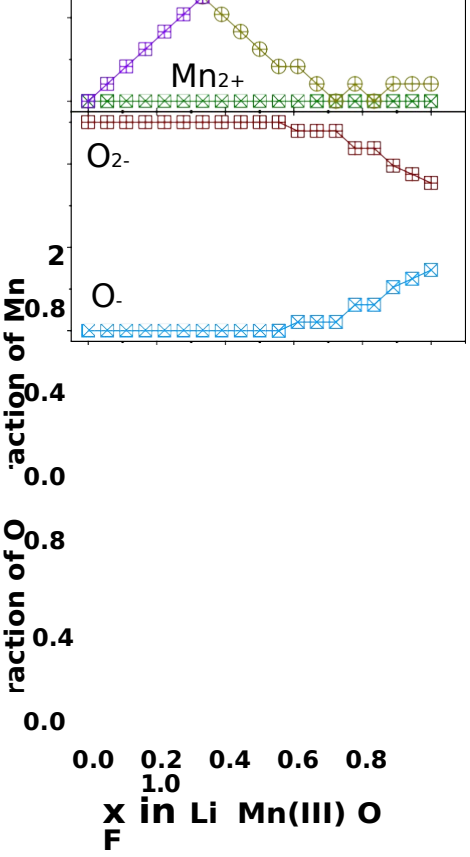
Mn2+
O2-
O-

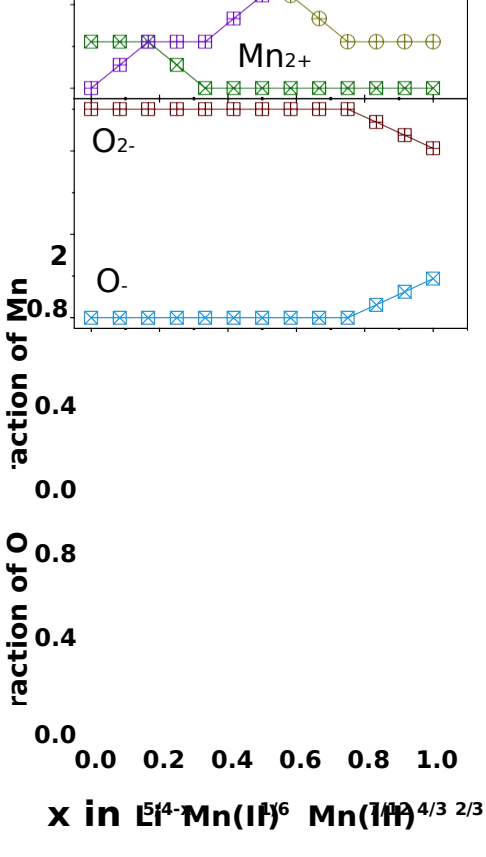
Mn2+
O2-
O-

raction of Mn
raction of O
0.0
0.4
0.8
2
0.8
0.4
0.0
0.0
0.2
0.4
0.6
0.8
1.0
x in Li Mn(III) O F
4/3-
2/3
4/3
2/3
x

raction of Mn
raction of O
0.0
0.4
0.8
2
0.8
0.4
0.0
0.0
0.2
0.4
0.6
0.8
1.0
x in Li Mn(II) Mn(III) O F
5/4-x
1/6
7/12
4/3
2/3

Figure 3 | Redox mechanism of Li-Mn-O-F compounds. a. Mn K-edge XANES spectra of all compounds at the pristine state and top charge in the first cycle. **b.** Mn K-edge XANES spectra of HLF67 and LLF67 at different states of charge in the initial cycle. Computed voltage profiles and evolution of Mn and O oxidation states calculated from DFT, denoting the dominant electron capacity source at each state of delithiation for **c.** HLF67 and **d.** LLF67. The experimental voltage profiles overlaid in the figures of each compound are the quasi-equilibrium voltage profiles obtained from potentiostatic intermittent titration technique (PITT) measurements when charged from open circuit voltage to 4.8 V.

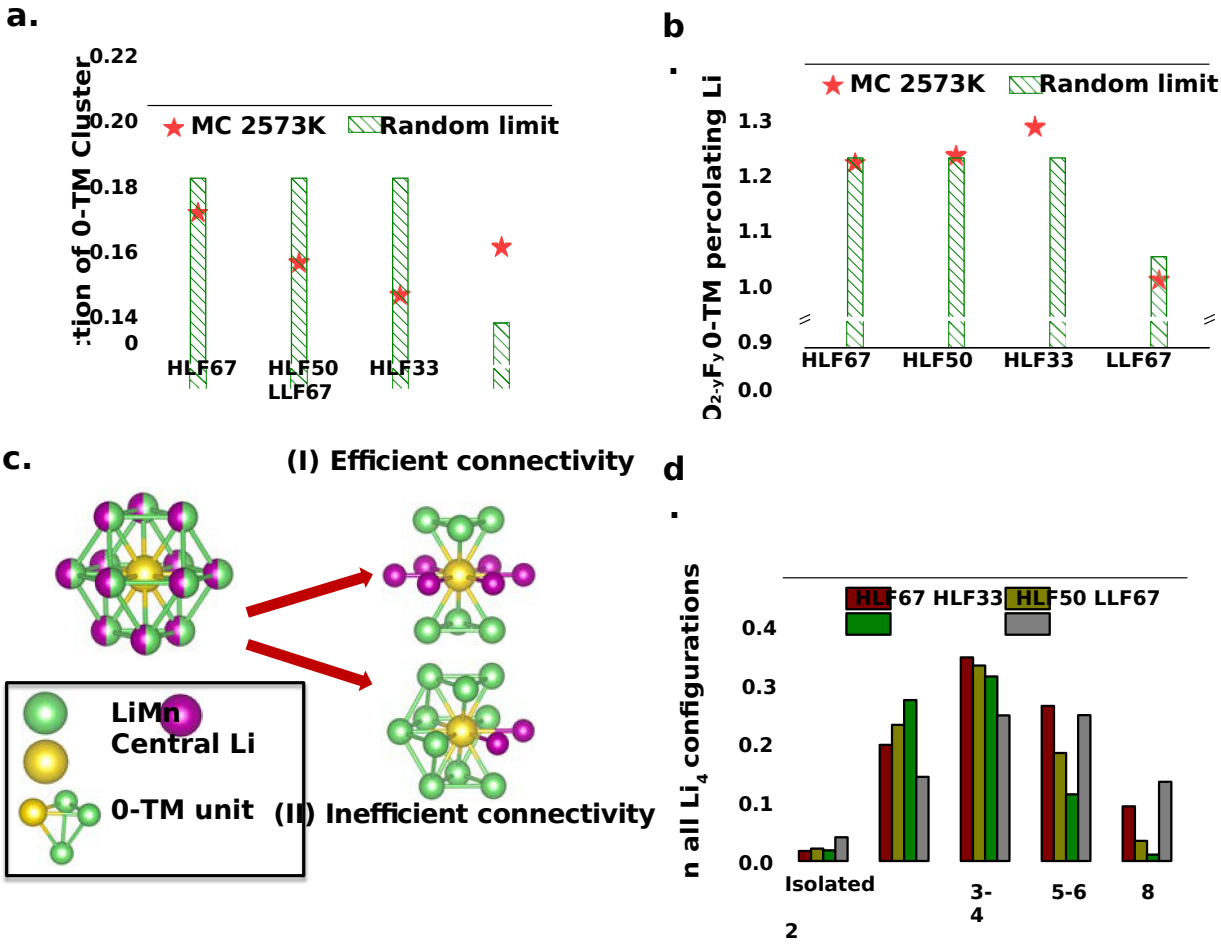

Figure 4 | SRO analysis of Li–Mn–O–F compounds. a. Fraction of 0-TM tetrahedral clusters in Li–Mn–O–F compounds obtained from the simulated MC structures at 2573K and random limit (infinite temperature). **b.** Amount of 0-TM-connected Li (percolating Li) per formula unit and comparison with random limits in Li–Mn–O–F compounds. **c.** Illustration of representative local bonding configurations around a central Li (highlighted in yellow), with green spheres and purple spheres referring to Li and Mn ions respectively. Configuration (I) presents an 'efficient' Li connectivity with the central Li shared by two 0-TM units; configuration (II) presents an 'inefficient' way to create an extended percolation network, where five 0-TM units are highly localized. **d.** Distribution of different bonding environments around all the Li that are presented in 0-TM tetrahedrons: the x-axis represents the number of 0-TM units one Li is shared by.

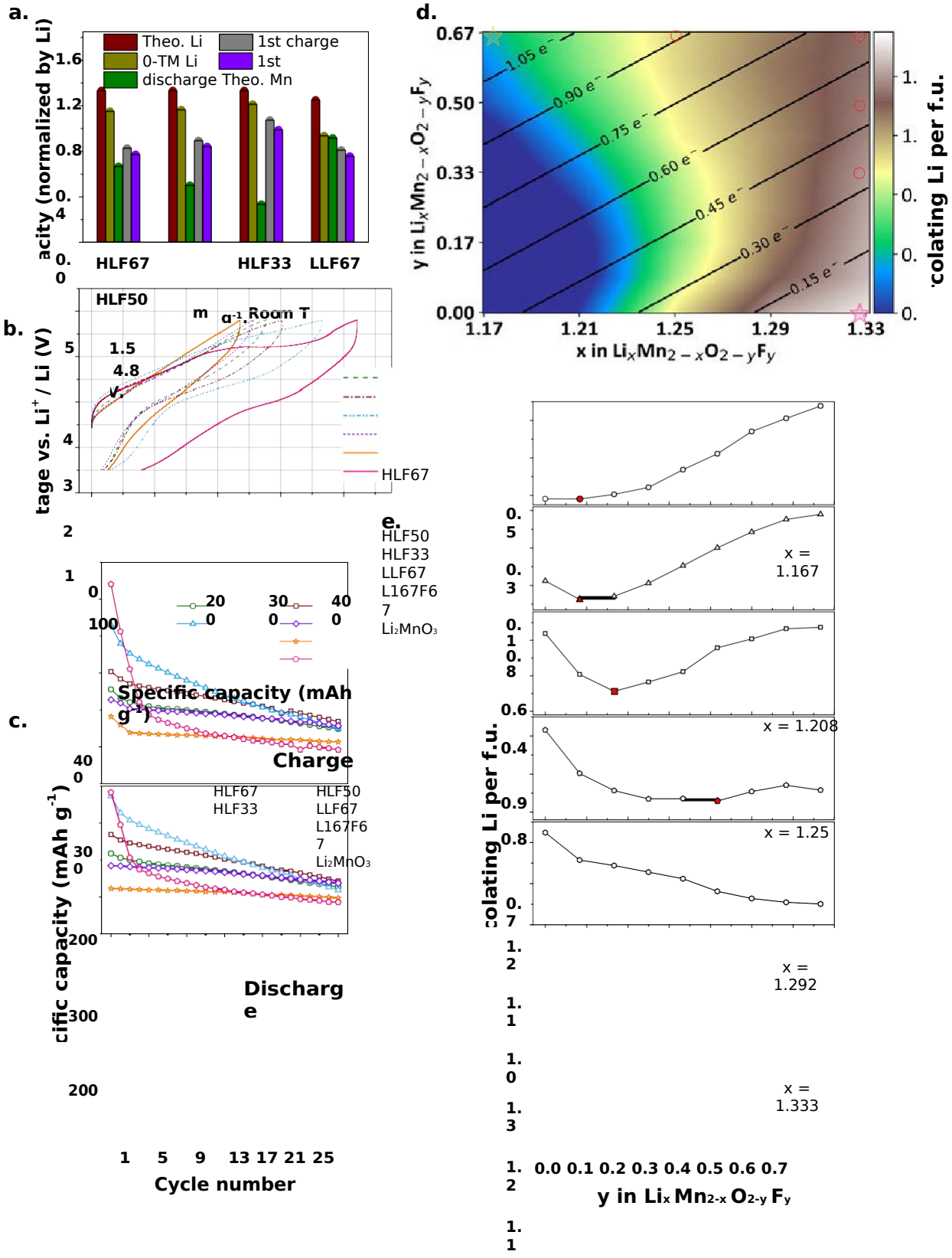

1

2 **Figure 5 | Design analysis for Li-Mn-O-F compounds. a.** Comparison of the theoretical Li/Mn-

redox capacities, accessible 0-TM capacities predicted by Monte Carlo simulations, and

experimental capacities obtained from the first charge/discharge at 20 mA g^{-1} and room

temperature within the voltage window of 1.5-4.8V for HLF67, HLF50, HLF33, LLF67.

Experimental first cycle **b.** voltage profiles and **c.** cyclability for all the Li–Mn–O–F compounds

at 20 mA g^{-1} and room temperature within a voltage window of 1.5-4.8V. **d.** Design map within

the Li-Mn-O-F DRX space. The color scale maps the total amount of percolating Li per formula

unit (f.u.) through 0-TM percolation network at each composition, obtained from Monte Carlo simulations at 2573K. The solid lines and numbers in the map indicate the theoretical Mn-redox capacity. The red circles mark the compositions that are studied in previous sections. The pink and yellow stars mark the composition with the highest amount of 0-TM Li (DRX-Li_2MnO_3) and the highest Mn-redox capacity ($L_{167}F_{67}$, $Li_{1.1667}Mn(II)_{0.3333}Mn(III)_{0.5}O_{1.3333}F_{0.6667}$) in the map, respectively. **e.** Li percolation analyses in $Li_xMn_{2-x}O_{2-y}F_y$ as a function of F (y values) at various Li-excess levels (x values). The critical F contents (local minimum) are highlighted in red.

References

1. Kang, K., Meng, Y.S., Bréger, J., Grey, C.P., and Ceder, G. (2006). Electrodes with High Power and High Capacity for Rechargeable Lithium Batteries. Science *311*, 977-980.
2. Xu, B., Qian, D., Wang, Z., and Meng, Y.S. (2012). Recent progress in cathode materials research for advanced lithium ion batteries. Materials Science and Engineering: R: Reports *73*, 51-65.
3. Turcheniuk, K., Bondarev, D., Singhal, V., and Yushin, G. (2018). Ten years left to redesign lithium-ion batteries (Nature Publishing Group).
4. Olivetti, E.A., Ceder, G., Gaustad, G.G., and Fu, X. (2017). Lithium-ion battery supply chain considerations: analysis of potential bottlenecks in critical metals. Joule *1*, 229-243.
5. Lee, J., Urban, A., Li, X., Su, D., Hautier, G., and Ceder, G. (2014). Unlocking the potential of cation-disordered oxides for rechargeable lithium batteries. Science *343*, 519-522.
6. Urban, A., Lee, J., and Ceder, G. (2014). The Configurational Space of Rocksalt-Type Oxides for High-Capacity Lithium Battery Electrodes. Advanced Energy Materials *4*, 1400478.
7. Yabuuchi, N. (2019). Material Design Concept of Lithium-Excess Electrode Materials with Rocksalt-Related Structures for Rechargeable Non-Aqueous Batteries. The Chemical Record *19*, 690-707.
8. Lee, J., Kitchaev, D.A., Kwon, D.-H., Lee, C.-W., Papp, J.K., Liu, Y.-S., Lun, Z., Clément, R.J., Shi, T., McCloskey, B.D.*, et al.* (2018). Reversible Mn2+/Mn4+ double redox in lithium-excess cathode materials. Nature *556*, 185-190.
9. Lee, J., Seo, D.-H., Balasubramanian, M., Twu, N., Li, X., and Ceder, G. (2015). A new class of high capacity cation-disordered oxides for rechargeable lithium batteries: Li–Ni–Ti–Mo oxides. Energy & Environmental Science *8*, 3255-3265.
10. Freire, M., Kosova, N., Jordy, C., Chateigner, D., Lebedev, O., Maignan, A., and Pralong, V. (2016). A new active Li–Mn–O compound for high energy density Li-ion batteries. Nature materials *15*, 173.
11. Glazier, S.L., Li, J., Zhou, J., Bond, T., and Dahn, J. (2015). Characterization of disordered Li (1+ x) Ti2 x Fe (1–3 x) O2 as positive electrode materials in Li-Ion batteries using

percolation
29 theory. Chemistry of Materials *27*, 7751-7756.
30 12. Chen, R., Ren, S., Knapp, M., Wang, D., Witter, R., Fichtner, M., and Hahn, H. (2015).
31 Disordered Lithium-Rich Oxyfluoride as a Stable Host for Enhanced Li+ Intercalation Storage.
32 Advanced Energy Materials *5*, 1401814-n/a.
33 13. Lun, Z., Ouyang, B., Kitchaev, D.A., Clément, R.J., Papp, J.K., Balasubramanian, M., Tian,
34 Y., Lei, T., Shi, T., McCloskey, B.D.*, et al.* (2019). Improved Cycling Performance of Li-Excess
35 Cation-Disordered Cathode Materials upon Fluorine Substitution. Advanced Energy Materials *9*,
36 1802959.
37 14. Kitchaev, D.A., Lun, Z., Richards, W.D., Ji, H., Clément, R.J., Balasubramanian, M.,
38 Kwon, D.-H., Dai, K., Papp, J.K., Lei, T.*, et al.* (2018). Design principles for high transition metal
39 capacity in disordered rocksalt Li-ion cathodes. Energy & Environmental Science *11*, 2159-2171.
40 15. House, R.A., Jin, L., Maitra, U., Tsuruta, K., Somerville, J.W., Förstermann, D.P., Massel,
41 F., Duda, L., Roberts, M.R., and Bruce, P.G. (2018). Lithium manganese oxyfluoride as a new
42 cathode material exhibiting oxygen redox. Energy & Environmental Science *11*, 926-932.
43 16. Hoshino, S., Glushenkov, A.M., Ichikawa, S., Ozaki, T., Inamasu, T., and Yabuuchi, N.
44 (2017). Reversible three-electron redox reaction of Mo3+/Mo6+ for rechargeable lithium batteries.
45 ACS Energy Letters *2*, 733-738.

17. Yabuuchi, N., Takeuchi, M., Nakayama, M., Shiiba, H., Ogawa, M., Nakayama, K., Ohta, T., Endo, D., Ozaki, T., Inamasu, T., *et al.* (2015). High-capacity electrode materials for rechargeable lithium batteries: Li3NbO4-based system with cation-disordered rocksalt structure. Proceedings of the National Academy of Sciences *112*, 7650-7655.
18. Lee, J., Papp, J.K., Clément, R.J., Sallis, S., Kwon, D.-H., Shi, T., Yang, W., McCloskey, B.D., and Ceder, G. (2017). Mitigating oxygen loss to improve the cycling performance of high capacity cation-disordered cathode materials. Nature communications *8*, 981.
19. Reed, J., Ceder, G., and Van Der Ven, A. (2001). Layered-to-Spinel Phase Transition in Li x MnO2. Electrochemical and Solid-State Letters *4*, A78-A81.
20. Richards, W.D., Dacek, S.T., Kitchaev, D.A., and Ceder, G. (2018). Fluorination of Lithium-Excess Transition Metal Oxide Cathode Materials. Advanced Energy Materials *8*, 1701533.
21. Clément, R.J., Kitchaev, D., Lee, J., and Gerbrand, C. (2018). Short-Range Order and Unusual Modes of Nickel Redox in a Fluorine-Substituted Disordered Rocksalt Oxide Lithium-Ion Cathode. Chemistry of Materials *30*, 6945-6956.
22. Kan, W.H., Deng, B., Xu, Y., Shukla, A.K., Bo, T., Zhang, S., Liu, J., Pianetta, P., Wang, B.-T., and Liu, Y. (2018). Understanding the effect of local short-range ordering on lithium diffusion in Li1. 3Nb0. 3Mn0. 4O2 single-crystal cathode. Chem *4*, 2108-2123.
23. Ji, H., Urban, A., Kitchaev, D.A., Kwon, D.-H., Artrith, N., Ophus, C., Huang, W., Cai, Z., Shi, T., Kim, J.C., *et al.* (2019). Hidden structural and chemical order controls lithium transport in cation-disordered oxides for rechargeable batteries. Nature Communications *10*, 592.
24. Jones, M.A., Reeves, P.J., Seymour, I.D., Cliffe, M.J., Dutton, S.E., and Grey, C.P. (2019). Short-range ordering in a battery electrode, the ‘cation-disordered’rocksalt Li 1.25 Nb 0.25 Mn 0.5 O 2. Chemical Communications *55*, 9027-9030.
25. Shannon, R.D. (1976). Revised effective ionic radii and systematic studies of interatomic distances in halides and chalcogenides. Acta crystallographica section A: crystal physics, diffraction, theoretical and general crystallography *32*, 751-767.
26. Clément, R.J., Kitchaev, D., Lee, J., and Ceder, G. (2018). Short-range Order and Unusual Modes of Nickel Redox in a Fluorine-substituted Disordered Rocksalt Oxide Lithium-ion Cathode. Chemistry of Materials.
27. Oishi, M., Fujimoto, T., Takanashi, Y., Orikasa, Y., Kawamura, A., Ina, T., Yamashige,

32 H., Takamatsu, D., Sato, K., and Murayama, H. (2013). Charge compensation mechanisms in Li1.
33 16Ni0. 15Co0. 19Mn0. 50O2 positive electrode material for Li-ion batteries analyzed by a
34 combination of hard and soft X-ray absorption near edge structure. Journal of Power Sources *222*,
35 45-51.
36 28. Seo, D.-H., Lee, J., Urban, A., Malik, R., Kang, S., and Ceder, G. (2016). The structural
37 and chemical origin of the oxygen redox activity in layered and cation-disordered Li-excess
38 cathode materials. Nature chemistry *8*, 692.
39 29. Yabuuchi, N., Nakayama, M., Takeuchi, M., Komaba, S., Hashimoto, Y., Mukai, T., Shiiba,
40 H., Sato, K., Kobayashi, Y., and Nakao, A. (2016). Origin of stabilization and destabilization in
41 solid-state redox reaction of oxide ions for lithium-ion batteries. Nature communications *7*, 13814.
42 30. Farrow, C., Juhas, P., Liu, J., Bryndin, D., Božin, E., Bloch, J., Proffen, T., and Billinge,
43 S. (2007). PDFfit2 and PDFgui: computer programs for studying nanostructure in crystals. Journal
44 of Physics: Condensed Matter *19*, 335219.

31. O'Dell, L.A., Rossini, A.J., and Schurko, R.W. (2009). Acquisition of ultra-wideline NMR spectra from quadrupolar nuclei by frequency stepped WURST–QCPMG. Chemical physics letters *468*, 330-335.
32. Pell, A.J., Clément, R.J., Grey, C.P., Emsley, L., and Pintacuda, G. (2013). Frequency-stepped acquisition in nuclear magnetic resonance spectroscopy under magic angle spinning. The Journal of Chemical Physics *138*, 114201.
33. Sananes, M., Tuel, A., Hutchings, G., and Volta, J. (1994). Characterization of different precursors and activated vanadium phosphate catalysts by 31P NMR spin echo mapping. Journal of Catalysis *148*, 395-398.
34. Massiot, D., Farnan, I., Gautier, N., Trumeau, D., Trokiner, A., and Coutures, J.P. (1995). 71Ga and 69Ga nuclear magnetic resonance study of β-Ga2O3: resolution of four-and six-fold coordinated Ga sites in static conditions. Solid State Nuclear Magnetic Resonance *4*, 241-248.
35. Ravel, B., and Newville, M. (2005). ATHENA, ARTEMIS, HEPHAESTUS: data analysis for X-ray absorption spectroscopy using IFEFFIT. Journal of Synchrotron Radiation *12*, 537-541.
36. McCloskey, B.D., Bethune, D., Shelby, R., Girishkumar, G., and Luntz, A. (2011). Solvents' critical role in nonaqueous lithium–oxygen battery electrochemistry. The Journal of Physical Chemistry Letters *2*, 1161-1166.
37. McCloskey, B.D., Scheffler, R., Speidel, A., Bethune, D.S., Shelby, R.M., and Luntz, A. (2011). On the efficacy of electrocatalysis in nonaqueous Li–O2 batteries. Journal of the American Chemical Society *133*, 18038-18041.
38. McCloskey, B.D., Speidel, A., Scheffler, R., Miller, D., Viswanathan, V., Hummelshøj, J., Nørskov, J., and Luntz, A. (2012). Twin problems of interfacial carbonate formation in nonaqueous Li–O2 batteries. The journal of physical chemistry letters *3*, 997-1001.
39. Richards, W.D., Dacek, S.T., Kitchaev, D.A., and Ceder, G. (2018). Fluorination of Lithium-Excess Transition Metal Oxide Cathode Materials. Advanced Energy Materials *8*, 1701533.
40. Nelson, L.J., Hart, G.L.W., Zhou, F., and Ozoliņš, V. (2013). Compressive sensing as a paradigm for building physics models. Physical Review B *87*, 035125.
41. Kresse, G., and Furthmüller, J. (1996). Efficiency of ab-initio total energy calculations for metals and semiconductors using a plane-wave basis set. Computational Materials Science *6*, 15-50.
42. Kresse, G., and Joubert, D. (1999). From ultrasoft pseudopotentials to the projector

augmented-wave method. Physical Review B *59*, 1758-1775.
43. Dudarev, S.L., Botton, G.A., Savrasov, S.Y., Humphreys, C.J., and Sutton, A.P. (1998). Electron-energy-loss spectra and the structural stability of nickel oxide: An LSDA+U study. Physical Review B *57*, 1505-1509.
44. Wang, L., Maxisch, T., and Ceder, G. (2006). Oxidation energies of transition metal oxides within the GGA+U framework. Physical Review B *73*, 195107.
45. Metropolis, N., Rosenbluth, A.W., Rosenbluth, M.N., Teller, A.H., and Teller, E. (1953). Equation of State Calculations by Fast Computing Machines. The Journal of Chemical Physics *21*, 1087-1092.
46. Hastings, W.K. (1970). Monte Carlo sampling methods using Markov chains and their applications. Biometrika *57*, 97-109.
47. Sun, J., Ruzsinszky, A., and Perdew, J.P. (2015). Strongly Constrained and Appropriately Normed Semilocal Density Functional. Physical Review Letters *115*, 036402.

48. Kitchaev, D.A., Peng, H., Liu, Y., Sun, J., Perdew, J.P., and Ceder, G. (2016). Energetics of MnO2 polymorphs in density functional theory. Physical Review B *93*, 045132.

49. Zhang, Y., Kitchaev, D.A., Yang, J., Chen, T., Dacek, S.T., Sarmiento-Pérez, R.A., Marques, M.A.L., Peng, H., Ceder, G., Perdew, J.P.*, et al.* (2018). Efficient first-principles prediction of solid stability: Towards chemical accuracy. npj Computational Materials *4*, 9.

50. Ong, S.P., Richards, W.D., Jain, A., Hautier, G., Kocher, M., Cholia, S., Gunter, D., Chevrier, V.L., Persson, K.A., and Ceder, G. (2013). Python Materials Genomics (pymatgen): A robust, open-source python library for materials analysis. Computational Materials Science *68*, 314-319.